Received: 28 June 2022 | Revised: 12 October 2022 | Accepted: 12 December 2022

DOI: 10.1111/jace.18982

Journal of the American Ceramic Society

RESEARCH ARTICLE

A 3D oxalate-bridged [$Cu^{II}Fe^{II}$] coordination polymer as molecular precursor for $CuFe_2O_4$ spinel—photocatalytic features

Lidija Molčanov[1] | **Lidija Androš Dubraja**[2] | **Martina Vrankić**[1] | **Marijana Jurić**[2]

[1]Division of Materials Physics, Ruđer Bošković Institute, Zagreb, Croatia

[2]Division of Materials Chemistry, Ruđer Bošković Institute, Zagreb, Croatia

Correspondence
Marijana Jurić, Division of Materials Physics, Ruđer Bošković Institute, Bijenička cesta 54, 10000 Zagreb, Croatia.
Email: Marijana.Juric@irb.hr

Funding information
Croatian Science Foundation, Grant/Award Number: IP-2019-04-5742

Abstract

A 3D heterometallic oxalate-bridged coordination polymer $[Cu^{II}Fe^{II}_2(H_2O)(terpy)(C_2O_4)_3]_n$ (terpy = 2,2′:6′,2″-terpyridine) (**1**) was investigated both as photocatalyst for the organic dye removal and as a single-source precursor for the preparation of the copper ferrite ($CuFe_2O_4$) nanocrystals by thermal processing. The dual functionality of **1** was supported by the degradation of aqueous solutions of rhodamine B (RhB) and methylene blue (MB) solutions under visible (Vis) and ultraviolet (UV) light irradiation, powder X-ray diffraction data collection at room temperature, and the optical and scanning electron microscopy analyses. A close inspection of the X-ray diffraction patterns unveiled qualitative and quantitative information on the phase composition obtained after the single-source molecular precursor route to spinel oxide. By optimizing the temperature levels and setting the controlled heating rate at 6 h of holding time, the phase composition of thermal processing of **1** was evaluated—thermal treatment of **1** at 950°C for 6 h and a heating/cooling rate of 10°C min^{-1} resulted in the formation of solely tetragonal spinel phase of $CuFe_2O_4$, whereas the formation of both tetragonal and cubic $CuFe_2O_4$ phases was observed at 950°C by the heating rate of 30°C min^{-1}. To obtain the high-temperature cubic $CuFe_2O_4$ oxide, compound **1** was heated and then quenched at 925°C, which led to the formation of the cubic spinel ferrite as the main crystalline oxide phase. Moreover, the photocatalytic properties of the *t*-$CuFe_2O_4$ spinel were investigated under the same conditions as for **1**. The optical bandgap energies were estimated from UV–Vis absorption spectra for both metal oxide and precursor powder.

KEYWORDS
bandgap, photocatalysis, precursors, spinels, thermal decomposition

1 INTRODUCTION

Metal–organic frameworks (MOFs) and coordination polymers (CPs) are being extensively studied for many potential applications ranging from the gas storage to molecular sieving, separation, ionic conductivity, and catalysis due to their structural diversity, high porosity, framework flexibility, large surface area, and tunable pore surface properties.[1–4] In recent years, much effort has been devoted to the development of new CPs and MOFs in the context of an efficient photocatalytic potential, including organic pollutant degradation, CO_2 reduction, and water splitting reaction toward H_2 production, utilizing ultraviolet (UV) and/or visible (Vis) lights. Nevertheless, a challenge in this field is to find an excellent photocatalyst that strongly absorbs sunlight and has a long excited-state lifetime and many charge-separating states with good charge mobility.[4–7]

Moreover, the use of heterometallic complexes or frameworks containing more than one metal as single-source precursors provides a simplified synthetic route through one-step thermal decomposition to form the mixed metal oxides. The advantage of a solid-phase transition is the retention of the elemental composition defined by the molecular precursor with only a loss of volatile decomposition products—allowing excellent stoichiometric control of the intermetallic ratio in the oxide products. It is known that the release of organic gases affects the particle size and porosity of the produced oxide; as the content of organics in the starting materials is increased, the larger porosity and smaller particle sizes in the decomposition products are more pronounced.[8–12] In addition, the impact of the temperature level and heating rate strongly correlates the thermal decomposition and prevention of the melting/vaporization of molecular species that can occur by rapid heating. Moreover, high temperature strongly affects the microstructural features (i.e., crystallite size, lattice strain, and porosity) of the produced material, thus narrowing the range between desired properties and cutting-edge applications. In particular, conventional ceramic processes that involve solid-state reactions using oxide, carbonate, or nitrate precursors often require processing at high temperatures, especially when highly crystalline products are needed. Undoubtedly, the high-temperature methods may lead to phase separation and/or yield only thermodynamic products.

The nanosized ferrites with the general formula MFe_2O_4 (M = Co, Cu, Mn, Ni, and Zn) exhibit good magnetic (i.e., high coercivity, high anisotropy, high Curie temperature, and moderate saturation magnetization), electrical (i.e., high electrical resistance and low eddy current losses), mechanical (i.e., significant mechanical hardness), and chemical (i.e., chemical stability and rich redox chemistry) properties that make them suitable for potential applications in the field of magnetic and dielectric materials, photoluminescence, catalysis, corrosion protection, sensors, antimicrobial agents, and biomedicine.[12–15] This spinel family has attracted much attention in energy conversion and storage applications due to its structural, physical, and chemical properties, which can be easily tuned and optimized for desired applications. This leads to cost-effective, efficient, environment-friendly, and versatile material systems for solar water splitting and environmental remediation (e.g., dye degradation). Magnetic ferrites have been previously prepared by a variety of wet synthesis methods, such as coprecipitation,[16–18] thermal decomposition,[18–20] sonochemical,[21,22] or solvothermal.[23,24] However, a key problem with much of the literature on is that the degree of control that these approaches have over the properties of the final product is poor. Namely, an implementation of such synthetic procedures induces the phase and stoichiometric heterogeneities and a rather lacking control over both microstructural features and morphological versatility. To date, there is no photocatalytic oxide material that meets all the practical requirements for successful operation as high durability, optimal narrow bandgap for full utilization of the entire solar spectrum, long lifetime of photogenerated electron–hole pairs, low cost, environmental friendliness, high efficiency, and stability. In this sense, it is extremely important to develop a rational design by optimizing the existing synthesis strategies, which may consequently lead to well-organized and visible-light-driven photocatalysts with a long lifetime.

This paper outlines the use of the CP $[Cu^{II}Fe^{II}_2(H_2O)(terpy)(C_2O_4)_3]_n$ (**1**; terpy = 2,2′:6′,2″-terpyridine)[25] as an efficient photocatalyst for the photodegradation of rhodamine B (RhB, $C_{28}H_{31}ClN_2O_3$) and methylene blue (MB, $C_{16}H_{18}N_3SC$) dye pollutants, as well as a single molecular precursor for the preparation of the $CuFe_2O_4$ spinel due to the suitable metal ratio by thermal treatment.[26–30] Namely, the oxalate group, $C_2O_4{}^{2-}$, easily decomposes at low temperatures into gaseous CO_2 and CO, and therefore, the oxalate-based solids can serve as suitable precursors for the preparation of mixed metal oxides.[11,26,28,31–33] In this work, we are the first ones to deliver a brief scheme on developing the feasible molecular precursor-to-material route for the preparation of $CuFe_2O_4$ spinel as viable alternative to various hydrothermal/solvothermal pathways. Structural and microstructural features of copper ferrite spinel were elucidated using powder X-ray diffraction (PXRD) measurements at room temperature (RT). Additionally, the morphological versatility of $CuFe_2O_4$ was characterized by scanning electron microscope (SEM) imaging. The impact of microstructural and morphological features of $CuFe_2O_4$ on the degradation of dye pollutants was evaluated through the energy bandgap calculations from UV–Vis absorption spectra, measured for both metal oxide and precursor powder.

2 | EXPERIMENTAL PROCEDURES

2.1 | Materials and methods

2.1.1 | Preparation of $[Cu^{II}Fe^{II}_2(H_2O)(terpy)(C_2O_4)_3]_n$

Deep-green prismatic crystals of CP $[Cu^{II}Fe^{II}_2(H_2O)(terpy)(C_2O_4)_3]_n$ (**1**) were synthesized following the procedure described in more detail in Ref. [25].

2.1.2 | Preparation of $CuFe_2O_4$ spinel

Finely ground crystalline powder of **1** was heated up to a certain temperature level, in a furnace (Nabertherm, Model LHT 02/16) inside a platinum crucible from RT, held in air with optimized constant heating rates, and then cooled down to RT in the same manner. The temperature limits were set to 700, 800, 900, and 950°C at 6 h holding time, whereas the heating rates varied from 5 to 30°C min^{-1}. Moreover, the phase evolution of ferrite spinel was studied by rapid quench experiments with a heating rate of 10°C min^{-1} at 925°C for 6 h holding time.

2.2 | Powder X-ray diffraction measurements

The PXRD data at RT were collected in reflection mode using a monochromatic Cu K_α X-ray source ($\lambda = 1.54056$ Å) on the Malvern Panalytical Empyrean powder diffractometer in the scan range from 5° to 50° 2θ. Structure refinements against X-ray diffraction data were performed with the Rietveld algorithm[34] using the HighScore Plus program (version 4.1; PANalytical B. V.: Almelo, Netherlands. 2014).[35] Starting models for tetragonal and cubic $CuFe_2O_4$ were based on those of Balagurov et al.[36] A pseudo-Voigt profile function and a polynomial background with up to four coefficients were applied to the structure refinements. Additionally, the microstructural features (i.e., crystallite size and lattice microstrain) were extracted from the phase fitting method based on the change in profile widths compared to a standard sample, using the following formula:

$$D_l = \frac{180}{\pi} \frac{\Lambda}{\left(W_l - W_{\mathrm{std}}\right)^{1/2}}$$

where W_l and W_{std} are the refinable profile parameters W for sample I and standard, comprised in the function that describes a variation of profile full width at half maximum (FWHM) with the Bragg angle[37]:

$$\mathrm{FWHM}\ (\theta) = \left(U\tan^2\theta + V\tan\theta + W\right)^{1/2}$$

The quantitative phase analysis was performed using the theory described by Hill and Howard.[38]

2.3 | Surface morphology analysis

SEM was performed on JEOL thermal field emission SEM (model JSM 7000F) operated at 10 keV.

2.4 | UV–Vis spectroscopy measurements

The UV–Vis diffuse reflectance spectroscopy (DRS) was performed on a Shimadzu UV–Vis–NIR spectrometer (model UV-3600) equipped with an integrating sphere. Barium sulfate was used as a reference. The diffuse reflectance spectra were transformed using the Kubelka–Munk function, and the optical bandgaps were estimated from Tauc's plots.[39]

2.5 | Photocatalytic experiments

The photocatalytic activity of **1** and $CuFe_2O_4$ was tested at RT by degradation over both aqueous solutions of RhB and MB dyes under Vis or UV irradiation. For each reaction, 1.0 mg of the powder sample was dispersed in 6.0 ml of a 10 ppm aqueous RhB or MB dye solution. Molar ratios of RhB and MB to catalyst were 0.086 and 0.129, respectively. Prior to irradiation, the suspension was constantly stirred for 1 h in the dark to ensure the establishment of an adsorption/desorption equilibrium. Then, 14 UV lamps of 352 nm (8 W, Hitachi) or Vis lamps (Hg lamp, 8 W, 400–700 nm) were turned on to start photodegradation in a photoreactor (Luzchem LZC-4V). A magnetic stirrer was placed at the bottom of the cell to keep the mixture in complete suspension. After irradiation, aliquots of 3 ml volume were taken at regular intervals and centrifuged at 7000 rpm for 8 min. Photocatalytic degradation reactions were monitored by measuring the concentration of a degraded supernatant liquid as a function of irradiation time by UV–Vis absorption spectra using a UV–Vis spectrophotometer (Varian Cary 60). The concentrations of RhB and MB were determined by measuring their absorbance at 552 and 660 nm, respectively. Prior to the experiments, blank tests without photocatalysts were performed.

TABLE 1 The notation of samples, synthesis conditions, and results of phase analysis obtained from the Rietveld refinements against laboratory powder X-ray diffraction (PXRD) data collected at room temperature (RT)

Sample	Temperature level (°C)	Heating rate (°C min^{-1})	t-$CuFe_2O_4$ (wt.%)	c-$CuFe_2O_4$ (wt.%)	CuO (wt.%)	R_{wp}
S1	700	5	74.9	–	18.5	2.53
S2	800	5	84.2	6.2	9.7	2.17
S3	900	5	89.1	–	10.9	2.49
S4	950	5	89.4	–	10.6	3.25
S5	950	10	100	–	–	2.25
S6	950	30	70.1	29.9	–	1.91
S7[a]	925	10	–	90.3	9.7	4.14

[a] Laboratory PXRD data collected at ambient conditions after quenching the sample from 925°C to RT.

3 | RESULTS AND DISCUSSION

3.1 | Structural and microstructural features of $[Cu^{II}Fe^{II}_2(H_2O)(terpy)(C_2O_4)_3]_n$-to-$CuFe_2O_4$ route

Previously reported CP $[Cu^{II}Fe^{II}_2(H_2O)(terpy)(C_2O_4)_3]_n$ (**1**) contains the well-known 2D honeycomb layers $[Fe^{II}_2(C_2O_4)_3]_n^{2n-}$ bridged by paramagnetic $[Cu(H_2O)(terpy)]^{2+}$ cations, ultimately yielding a 3D network exhibiting long-range magnetic order (Figure S1). It is moderately stable in the solid state in air for a reasonable period of time. Its thermal behavior shows single-step decomposition ending around 600°C.[25]

By optimizing the temperature limits and setting the controlled heating rate at 6 h holding time, an effect of both temperature level and heating rate on the evolution of the phase composition of final products can be smoothly followed (Table 1). The heating of deep-green polycrystals of **1** (Figure S2) at 950°C for 6 h using heating rate of 10°C min^{-1}, led to a formation of a single-phase PXRD pattern of a tetragonal[36] $CuFe_2O_4$ spinel [s. g. $I4_1/amd$, $a = b = 5.8794(1)$ Å and $c = 8.5971(2)$ Å]. On the other hand, a smaller quantity of cubic[36] $CuFe_2O_4$ (s. g. Fd-$3m$, $a = 8.370$ Å) and monoclinic CuO were observed at 700, 800, 900, and 950°C at a heating rate of 5°C min^{-1}, as confirmed by the PXRD analysis (Figure 1). The presence of the CuO impurity phase is in agreement with the results obtained very much under the similar conditions as indicated in Refs. [40, 41].

Formation of both tetragonal and cubic $CuFe_2O_4$ was observed at 950°C by setting the heating rate to 30°C min^{-1}. Apparently, larger temperature levels and higher heating rates favor the formation of solely copper ferrite phase, as confirmed by the Rietveld-based quantitative results (Table 1). The initial Rietveld refinement of the structural model for S5 showed that the starting crystal structure quite nicely fits the tetragonal[36] ferrite spinel [s. g. $I4_1/amd$, $a = b = 5.834(3)$ Å, $c = 8.689(5)$ Å, $V = 295.7(5)$ Å^3, $R_{wp} = 2.25\%$, $R_{exp} = 2.36\%$]. Further quantitative analysis of sample S6 revealed a two-phase pattern with both 70.1 wt.% tetragonal[36] $CuFe_2O_4$ [s. g. $I4_1/amd$, $a = b = 5.862(2)$ Å, $c = 8.592(4)$ Å, $V = 295.2(2)$ Å^3] and 29.9 wt.% cubic[36] $CuFe_2O_4$ [s. g. Fd-$3m$, $a = 8.418(3)$ Å, $V = 596.5(2)$ Å^3] giving discrepancy factors of $R_{wp} = 1.91\%$ and $R_{exp} = 1.94\%$. On the other hand, rapid quenching from 925°C to RT resulted in the formation of 90.3 wt.% cubic $CuFe_2O_4$ and 9.7 wt.% CuO as impurity phase in sample S7 (see Figure S3). Figure 2 shows a comparison of structural fits for S5 and S6 powder patterns. As expected, a significant correlation between synthetic conditions and microstructural evolution was also observed. Namely, the calculated crystallite sizes tended to increase with the temperature level and heating rate. The values of crystallite sizes for the t-$CuFe_2O_4$ phase obtained from the line-broadening analysis performed during the structure refinements increased from 34.4(1) nm in sample S5, annealed at 950°C, and cooled down to RT at a heating rate of 10°C min^{-1} to 45.6(1) nm in sample S6, which was annealed at 950°C and cooled down to RT at a heating rate of 30°C min^{-1} (Figure 2). Similarly, the average crystallite size of 35.6(1) nm was calculated for the c-$CuFe_2O_4$ phase in sample S6. Our microstructural results share similarities with Zakiyah et al.'s findings,[42] according to which the crystallite sizes were found to increase linearly with the calcination temperature, from 23 nm at 500 K to 33 nm at 900°C. Simultaneously, the lattice strains of 0.25% for tetragonal phase remained unchanged upon increasing the heating rate from 10 to 30°C min^{-1} in S5 and S6, respectively. Additionally, the calculated lattice strains for the cubic phase in S6 showed a similar value of 0.27%.

3.2 | Surface morphology imaging

The surface morphology of samples obtained by heating metal–organic precursor **1** up to 950 and 925°C at a heating

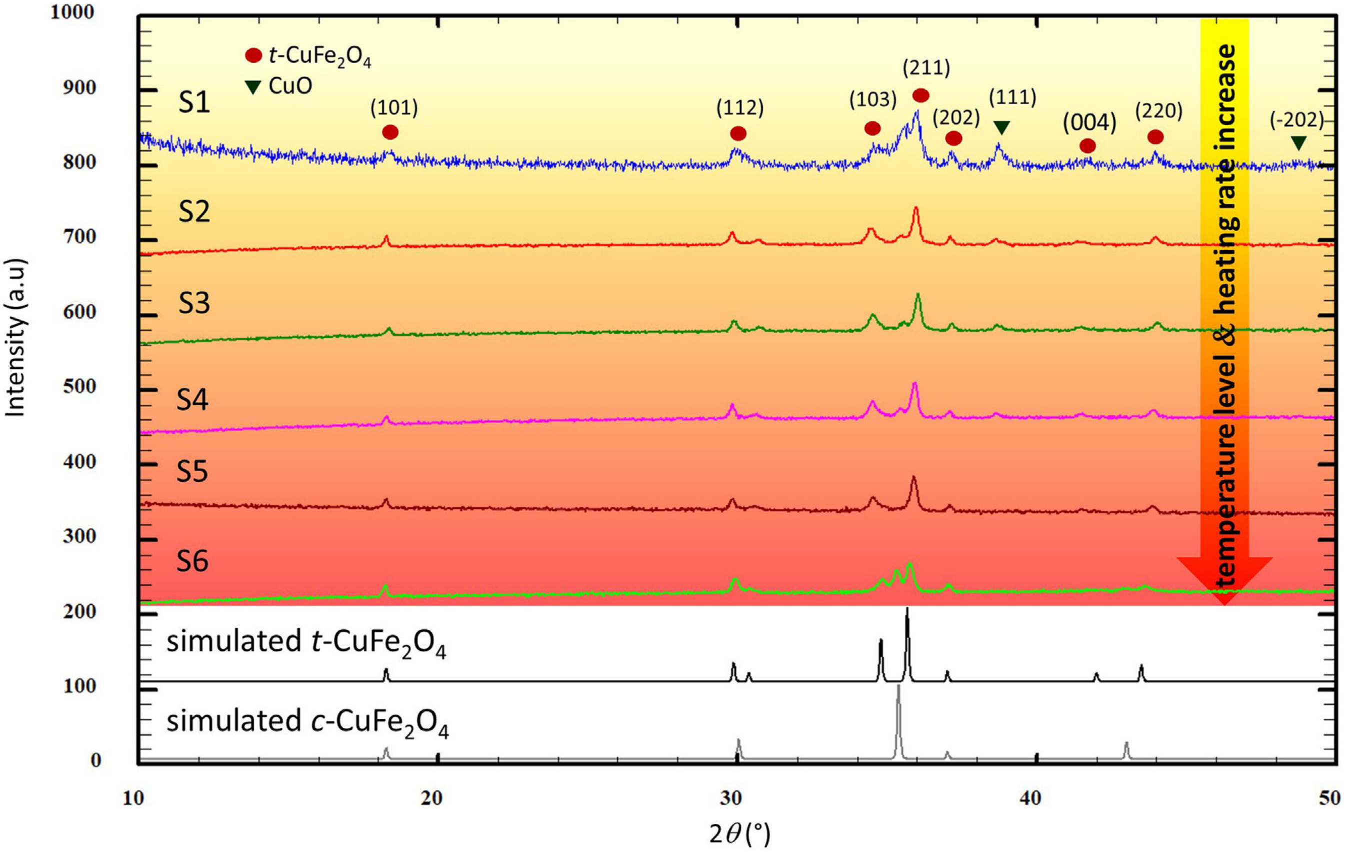

FIGURE 1 Cascade powder X-ray diffraction (PXRD) patterns at room temperature (RT) of samples S1–S6 prepared at temperatures and heating rates listed in Table 1. The experimental data for the ferrite phase are corroborated by the simulated PXRD patterns (bottom) of t-$CuFe_2O_4$ and c-$CuFe_2O_4$ collected at ambient conditions

rate of 10°C min^{-1} and holding time 6 h, and subsequent controlled cooling with 10°C min^{-1} rate and quenching, designated as samples S5 and S7, are shown in parts (A) and (B) of Figure 3, respectively. Morphological differences between samples S5 (tetragonal phase) and S7 (cubic phase) are clearly visible from the SEM images and can be correlated with the cooling rate. Cubic $CuFe_2O_4$ phase that was prepared by quenching from 925°C crystallizes in a regular octahedral morphology (Figure 3B), whereas crystals of tetragonal $CuFe_2O_4$, prepared by controlled cooling, adopt a truncated octahedron geometry (Figure 3A). It appears that slower cooling rates (10°C min^{-1} vs. quenching) propagate the growth of {1 0 0} faces and the evolution of the primary $CuFe_2O_4$ from octahedron to truncated octahedron shape. The particle size distribution ranges from 0.1 to 10 μm for both ferrite samples (Figure S4), thus indicating on an agglomeration of nanosized crystallites calculated from the phase fit method against PXRD data. In addition to relatively large particles, micrographs also indicate negligible interparticle porosity. It is indisputable that such morphological properties limit the performance of prepared ferrites for photocatalytic and other surface-area-dependent applications. As these morphological results differ considerably from those of Zakiyah et al.,[42] it could nevertheless be argued that the use of capping agents[43] stabilizes and inhibits the overgrowth of copper ferrites nanoparticles and prevent their aggregation in the synthesis, thus playing a key role in the morphological evolution of $CuFe_2O_4$ nanoparticles.

3.3 | UV–Vis spectroscopy measurements

The optical properties of both **1** and sample S5 were analyzed by UV–Vis DRS. The Kubelka–Munk diffuse reflectance absorption spectrum of **1**, shown in Figure 4A, reveals the strongest bands in the visible part of the spectrum located at 480 and 665 nm. These bands are the characteristic of the ligand-to-metal charge transfer in the $Fe^{II}(C_2O_4)_3$ octahedra and d–d transitions of the elongated $Cu(terpy)(H_2O)(C_2O_4)$ octahedra, respectively.[44] Tauc's plots from diffuse reflectance measurements (Figure 4B) show multiple absorption peaks or edges, which are often present in hybrid polyfunctional materials, for example, MOFs.[45] The indirect bandgap can be estimated in the photon energy of about 1.52 eV and larger direct bandgap

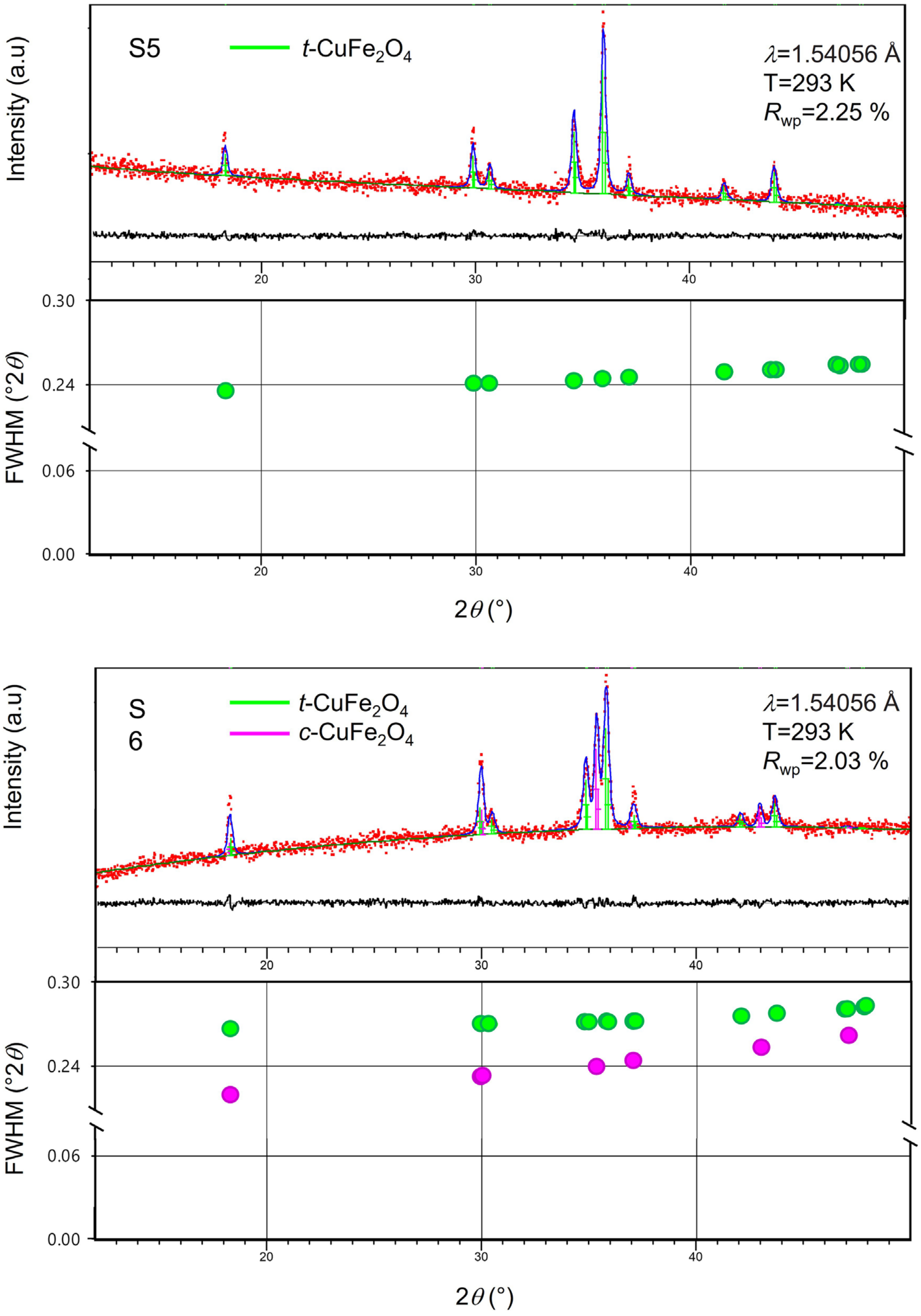

FIGURE 2 Final observed (red dots) and calculated (blue solid line) powder diffraction profiles along with the line broadening analysis of samples S5 and S6, prepared at temperatures and heating rates listed in Table 1 as obtained from the Rietveld refinements against powder X-ray diffraction (PXRD) data at room temperature (RT). The fitted background contribution is represented by the lower deep-green solid line. The black solid line (bottom) shows the difference profile, whereas the green and purple vertical lines depict the reflection positions of tetragonal and cubic $CuFe_2O_4$, respectively

energy close to 2.46 eV. Based on the optical (direct or indirect) bandgap energies, compound **1** is a good candidate as photocatalyst for degradations of pollutants or splitting of H_2O under visible light irradiation.

Copper ferrite has been recently reported as potential candidate for photoanode, exhibiting the narrow bandgap of 1.3–2 eV.[46–48] We have performed diffuse reflectance measurements, and from the Kubelka–Munk transformation spectra, it is evident that sample S5 shows no absorption bands in the visible light region (Figure S5). Moreover, the optical bandgap energy for this sample was estimated to be 1.32(1) eV. Such a small value of optical

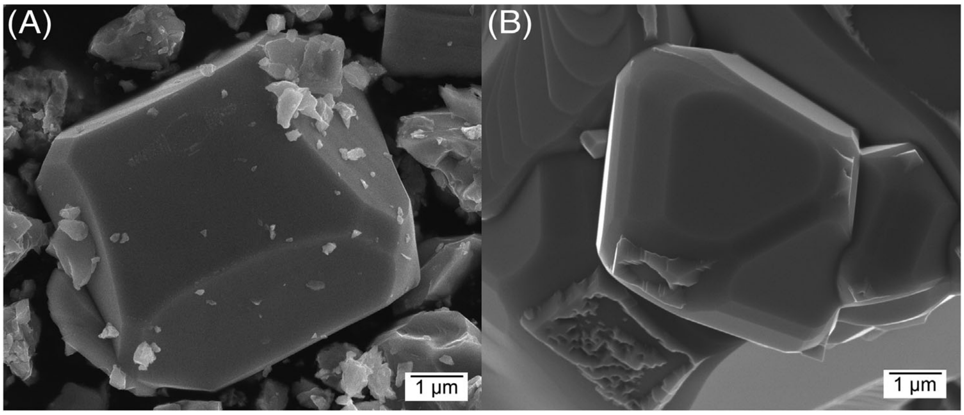

FIGURE 3 Scanning electron microscopy (SEM) images of tetragonal S5 (A) and cubic S7 (B) $CuFe_2O_4$ spinel prepared from molecular precursor **1**

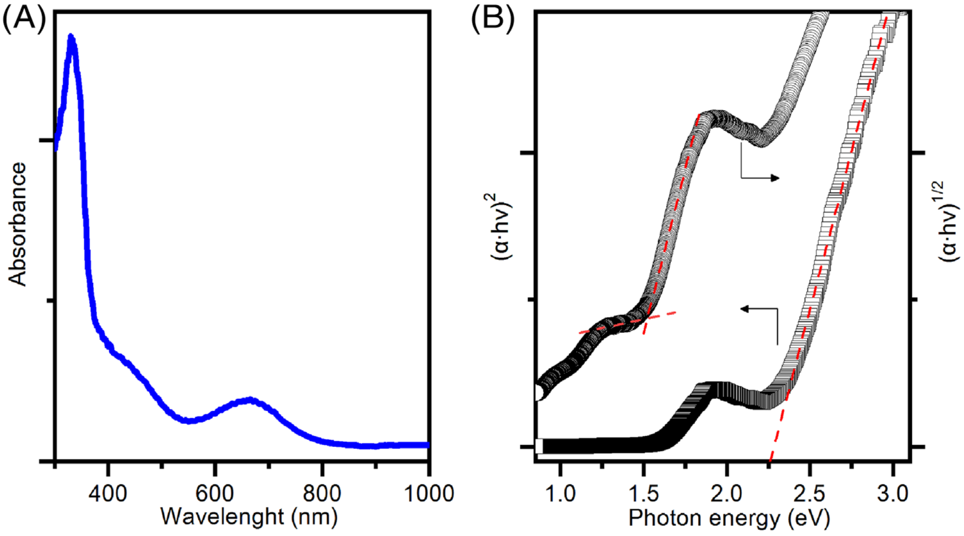

FIGURE 4 Kubelka–Munk diffuse reflectance absorption spectrum of **1** (A), and direct and indirect optical transitions (B). Dashed red lines indicate the bandgap energies

bandgap is directly reflected by the particle agglomeration effect, corroborated by SEM micrographs. For comparison, the direct optical bandgap of 2.61 eV was obtained for $CuFe_2O_4$ prepared using the capping agent and calcined at 900°C in Ref. [43]. Generally, the optical bandgap is found to decrease with an increase of particle size as a result of increasing calcination temperature.

3.4 | Photocatalytic degradation of RhB and MB dye pollutants

Deep-green polycrystals of **1** did not show the lack of stability in water and under both UV and Vis irradiations. Namely, **1** adsorbed in the dark to reach an equilibrium of photocatalytic testing (19.89% in MB and 28.70% in RhB). The decomposition efficiency for MB increased from 3.17% (control experiment) to 63.37% under UV, and from 15.87% to 60.23% under Vis irradiation, after 120 min. The degradation of RhB increased from 3.56% (without photocatalyst) to 64.9% under UV, and from 1.4% to 44.47% under Vis irradiation, after 120 min. As seen from Figure 5A–D, the maximum absorption peaks of solutions of MB and RhB under Vis and UV light in the presence of compound **1** as photocatalyst decreased with the reaction time showing a good photocatalytic performance of this compound. The control experiments on the degradation of MB and RhB dye solutions without photocatalysts are shown in Figure 5E,F. Unfortunately, the recyclability and stability test of **1** for the reduction of dye pollutants did not show good results, as the second run showed no photocatalytic performance.

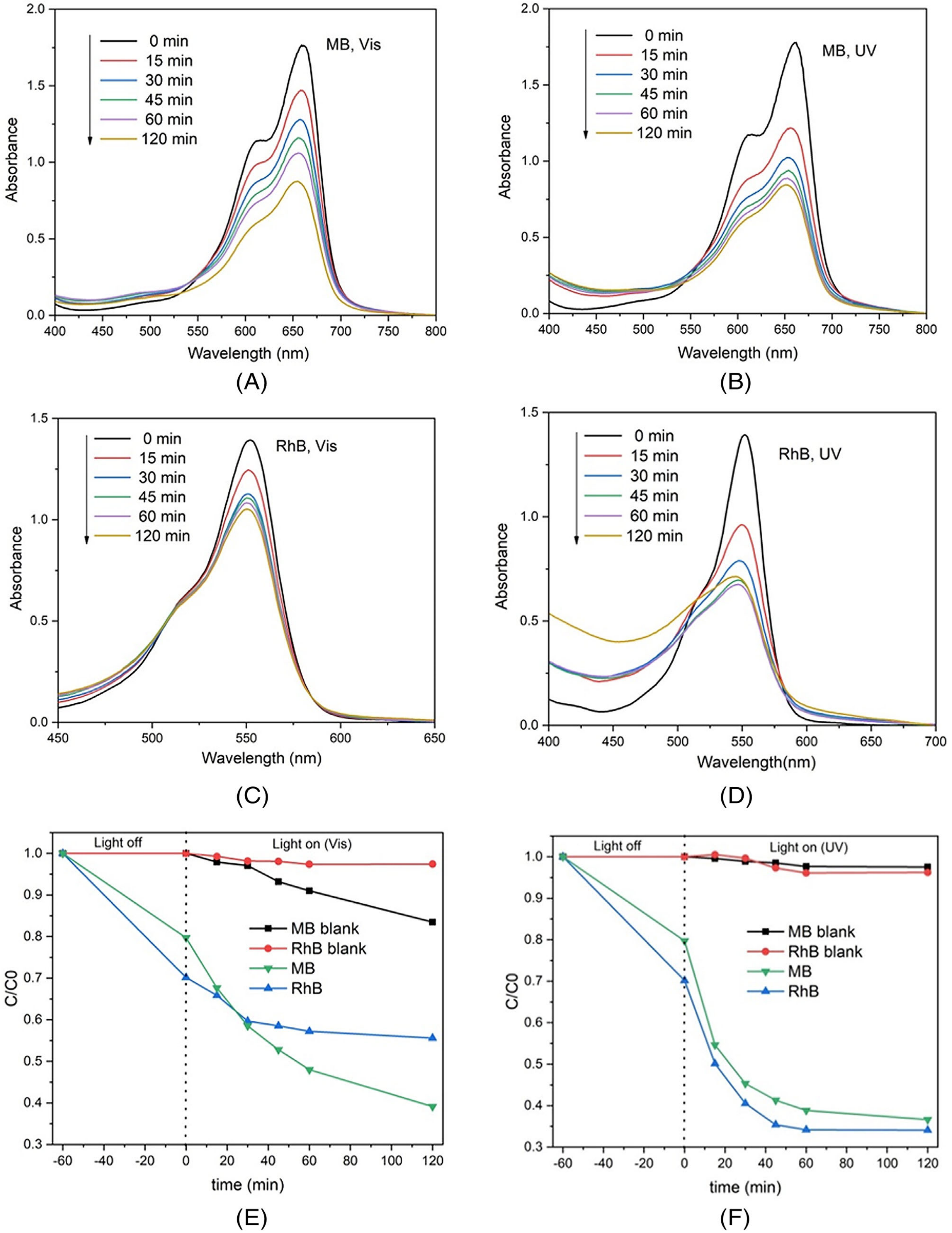

FIGURE 5 Ultraviolet–visible (UV–Vis) absorption spectra of methylene blue (MB) solution during the decomposition reaction in the presence of **1** under: (A) Vis and (B) UV light irradiations; UV–Vis absorption spectra of rhodamine B (RhB) solution during the decomposition reaction in the presence of **1** under: (C) Vis and (D) UV light irradiation; plots of concentration versus irradiation time for MB and RhB using **1** as photocatalyst before and under: (E) Vis and (F) UV light irradiations

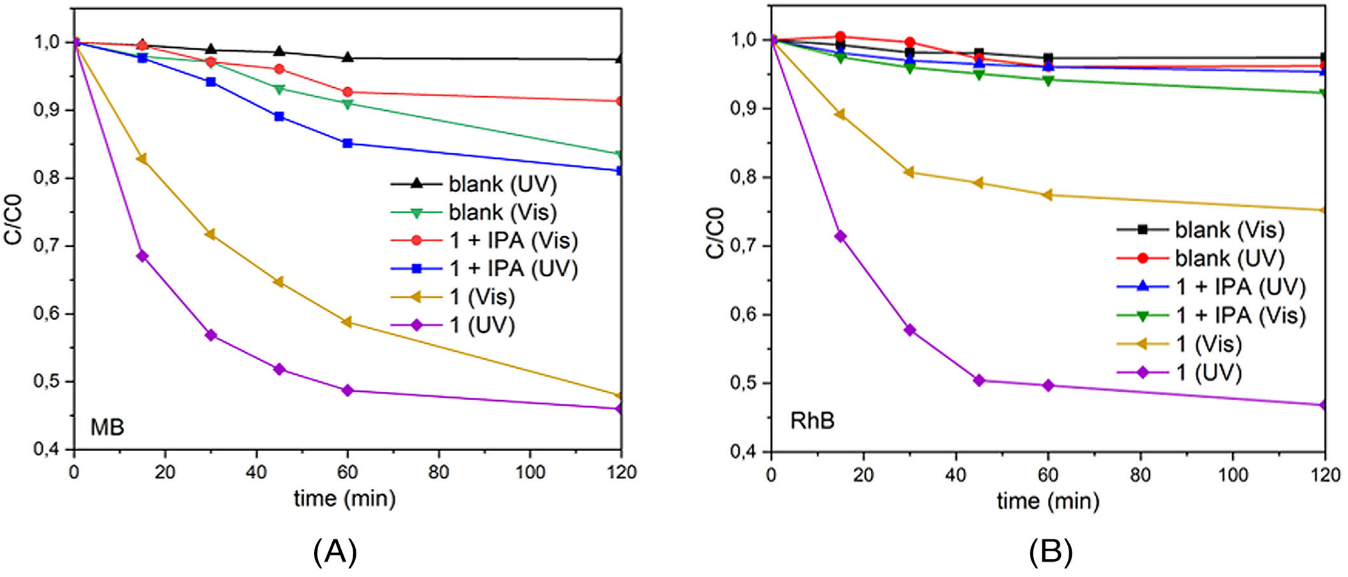

FIGURE 6 Photocatalytic efficiencies of the solution methylene blue (MB) (A) and rhodamine B (RhB) (B) under ultraviolet (UV) and visible (Vis) light irradiation using **1** as the photocatalyst, in the presence of IPA as a radical scavenger and blank

In metal–organic compounds exhibiting photocatalytic behavior, charge transfer generally occurs from the HOMO, including O and/or N atoms, to the LUMO, including metal atom; HOMO of the excited species usually accepts one electron, whereas the excited-state electron in the LUMO is easily lost. Water molecules capture electrons and generate active $^{\bullet}$OH species that destroy organic dye during photocatalytic process.[5,6,49,50] Thus, according to the mechanism proposed for the host–guest system and CPs such as $\{[Z^{II/III}(bpy)_3][M^{I}M^{III}(C_2O_4)_3]\}_n$,[51] it is also very likely that structural unit $[Fe^{II}{}_2(C_2O_4)_3]^{2-}$ of **1** enters its excited state under light irradiation. Moreover, the cationic species $[Cu(H_2O)(terpy)]^{2+}$ is excited by the resonant energy migration from the exited anionic unit. The excited species $[Cu(H_2O)(terpy)]^{2+}$ transfer an electron, located on the terpy ligand, to the water proton and generate the $^{\bullet}$OH active species. To confirm the proposed reaction mechanism of photocatalytic degradation responsible for the decomposition of dyes, radical trapping experiments were performed to identify the major oxidative species in the photocatalytic process.[52–55] Photodegradation was performed in the presence of isopropanol (IPA), which act as a quencher of $^{\bullet}$OH radicals. The addition of 1 mM IPA significantly inhibited the degradation efficiency for MB (decrease from 63.37% without IPA to 18.19% with IPA under UV, and from 60.23% without IPA to 8.55% with IPA under Vis irradiation), and RhB (decrease from 64.9% without IPA to 4.63% with IPA under UV, and from 44.47% to 7.71% with IPA) after 120 min, as shown in Figures 6 and S6. These results support the role of $^{\bullet}$OH radicals as the main active species during the degradation process.

Despite the poor recyclability and stability of compound **1**, the first cycle of the photocatalytic experiment showed non-negligible results that could be important due to the lack of photocatalytic characterization of similar compounds (containing two or more different metal centers) in the literature. Usually, homometallic compounds are tested for their photocatalytic activity. The decomposition rates of RhB or MB using compound **1** as photocatalyst could be compared to three polyoxometalates (POMs)-based metal–organic complexes $[Mn_2(4\text{-pdtz})_2[CrMo_6(OH)_5O_{19}](H_2O)_4]$, $\{Mn(3\text{-dpye})_{0.5}[CrMo_6(OH)_6O_{18}](H_2O)\}\cdot(3\text{-}H_2dpye)_{0.5}$, and $[Mn_2(3\text{-}H_2dpye)(TeMo_6O_{24})(H_2O)_6]\cdot 4H_2O$ (4-pdtz = 4-pyridino-bistriazol, 3-dpye = *N*,*N*′-bis(3-pyridinecarboxamide)-1,2-ethane). They show good photocatalytic activity; the degradations of MB 67.5%–96.6% under UV and 55.9%–93.7% under Vis irradiation, and those of RhB 42.1%–58.9% under UV and 42.2%–56.5% under Vis light, have been observed.[56] Furthermore, the 2D polymer complex, $\{[K(NiL)]\cdot x CH_3CN\}_n$ (H_3L = 5-nitrosalicylaldehyde-based ligand), showed a photodegradation of MB with 69% in 1 h under the irradiation of UV–Vis light.[57] All presented results reveal that compound **1** shows comparable photocatalytic activity toward the degradation of RhB and MB dyes under UV and Vis lights compared to known heterometallic CPs.

Additionally, the photocatalytic properties of the *t*-$CuFe_2O_4$ spinel (sample S5) were examined under the same conditions as for **1**. However, our findings do not support previous research in this area. Namely, contrary to the results of previous studies,[58–60] we found no photocatalytic activity of ferrite spinel over RhB and MB dye solutions, neither under UV nor under Vis light irradiation (Figure S7), which can be attributed to its large particle size and small bandgap.

4 | CONCLUSIONS

Rhodamine B and methylene blue dye pollutants were successfully degraded under UV and Vis light illuminations within 120 min, using the 3D CP $[Cu^{II}Fe^{II}_2(H_2O)(terpy)(C_2O_4)_3]_n$. Furthermore, this heterometallic oxalate-bridged assembly was for the first time successfully implemented in heat treatment, molecular precursor-to-material route, resulting in a phase-pure formation of tetragonal copper ferrite spinel at 950°C for 6 h and heating/cooling rate of 10°C min^{-1}, thus smoothly bypassing both the long-term heating and repeated grinding processes. Similarly, by setting the heating rate to 30°C min^{-1}, a mixture of tetragonal and cubic $CuFe_2O_4$ phases was observed at the same temperature level and holding time. In contrast with our earlier findings,[26] the present pathway shows some limitations. Namely, the catalytic and optical features of $CuFe_2O_4$ cannot be easily tuned, as the phase composition and the crystallite sizes cannot be controlled by altering the preparation conditions. Nevertheless, we succeeded in obtaining the copper ferrite as single phase, unlike $CuMn_2O_4$, which was obtained as major crystalline phase at 1000°C by heating of appropriate CP.[27] Thereby, this apparent lack of correlation between microstructural and optical characteristics, which is attributed mainly to the synthesis settings, represents an important issue to resolve for future studies. Further investigations on the current topic are therefore required in order to improve the suggested synthetic route and enhance structure–property relationship of precursor-to-material processed $CuFe_2O_4$ powder.

ACKNOWLEDGMENT

This work was funded and supported by the Croatian Science Foundation under project no. IP-2019-04-5742.

CONFLICTS OF INTEREST

The authors declare no conflicts of interest.

ORCID

Lidija Molčanov https://orcid.org/0000-0002-4062-6599
Lidija Androš Dubraja https://orcid.org/0000-0002-7648-4940
Martina Vrankić https://orcid.org/0000-0002-8461-221X
Marijana Jurić https://orcid.org/0000-0001-5951-9366

REFERENCES

1. Chakraborty G, Park I-H, Medishetty R, Vittal JJ. Two-dimensional metal-organic framework materials: synthesis, structures, properties and applications. Chem Rev. 2021;121:3751–91.
2. Chen L, Zhang X, Cheng X, Xie Z, Kuang Q, Zheng L. The function of metal–organic frameworks in the application of MOF-based composites. Nanoscale Adv. 2020;2:2628–47.
3. Wang Q, Astruc D. State of the art and prospects in metal-organic framework (MOF)-based and MOF-derived nanocatalysis. Chem Rev. 2020;120:1438–511.
4. Zhao S-N, Wang G, Poelman D, Van Der Voort P. Metal organic frameworks based materials for heterogeneous photocatalysis. Molecules. 2018;23:2947.
5. Wang Q, Gao Q, Al-Enizi AM, Nafady A, Ma S. Recent advances in MOF-based photocatalysis: environmental remediation under visible light. Inorg Chem Front. 2020;7:300–39.
6. Xiao J-D, Jiang H-L. Metal-organic frameworks for photocatalysis and photothermal catalysis. ACC Chem Res. 2019;52:356–66.
7. Reddy CV, Reddy KR, Harish VVN, Shim J, Shankar MV, Shetti NP, et al. Metal-organic frameworks (MOFs)-based efficient heterogeneous photocatalysts: synthesis, properties and its applications in photocatalytic hydrogen generation, CO_2 reduction and photodegradation of organic dyes. Int J Hydrogen Energy. 2020;45:7656–79.
8. Lu H, Wright DS, Pike SD. The use of mixed-metal single source precursors for the synthesis of complex metal oxides. Chem Commun. 2020;56:854–71.
9. Li M, Liu J, Liu T, Zhang M, Pan F. A versatile single molecular precursor for the synthesis of layered oxide cathode materials for Li-ion batteries. Chem Commun. 2018;54:1331–4.
10. Li M, Yang K, Liu J, Hu X, Kong D, Liu T, et al. A heterobimetallic single-source precursor enabled layered oxide cathode for sodium-ion batteries. Chem Commun. 2018;54:10714–7.
11. Jurić M, Popović J, Šantić A, Molčanov K, Brničević N, Planinić P. Single-step preparation of the mixed Ba^{II}–Nb^{V} oxides from a heteropolynuclear oxalate complex. Inorg Chem. 2013;52:1832–42.
12. Dippong T, Levei EA, Cadar O. Recent advances in synthesis and applications of MFe_2O_4 (M = Co, Cu, Mn, Ni, Zn) nanoparticles. Nanomaterials. 2021;11:1560.
13. Chandrasekaran S, Bowen C, Zhang P, Li Z, Yuan Q, Ren X, et al. Spinel photocatalysts for environmental remediation, hydrogen generation, CO_2 reduction and photoelectrochemical water splitting. J Mater Chem A. 2018;6:11078–104.
14. Androš Dubraja L, Reitz C, Velasco L, Witte R, Kruk R, Hahn H, et al. Electrochemical tuning of magnetism in ordered mesoporous transition-metal ferrite films for micromagnetic actuation. ACS Appl Nano Mater. 2018;1:65–72.
15. Zhao Q, Yan Z, Chen C, Chen J. Spinels: controlled preparation, oxygen reduction/evolution reaction application, and beyond. Chem Rev. 2017;10121–211.
16. Salavati-Niasari M, Mahmoudi T, Sabet M, Hosseinpour-Mashkani SM, Soofivand F, Tavakoli F. Synthesis and characterization of copper ferrite nanocrystals via coprecipitation. J Cluster Sci. 2012;23:1003–10.
17. Kanagaraj M, Sathishkumar P, Selvan GK, Kokila P, Arumugam S. Structural and magnetic properties of $CuFe_2O_4$ as-prepared

and thermally treated spinel nanoferrites. Indian J Pure Appl Phys. 2014;52:124–30.

18. Moshtaghi S, Ghanbari D, Salavati-Niasari M. Characterization of $CaSn(OH)_6$ and $CaSnO_3$ nanostructures synthesized by a new precursor. J Nanostruct. 2015;5:169–74.
19. Sharifi I, Zamanian A, Behnamghader A. Synthesis and characterization of $Fe_{0.6}Zn_{0.4}Fe_2O_4$ ferrite magnetic nanoclusters using simple thermal decomposition method. J Magn Magn Mater. 2016;412:107–13.
20. Al-Gaashani R, Aïssa B, Anower Hossain M, Radiman S. Catalyst-free synthesis of ZnO-CuO-$ZnFe_2O_4$ nanocomposites by a rapid one-step thermal decomposition approach. Mater Sci Semicond Process. 2019;90:41–9.
21. Gholami T, Salavati-Niasari M, Bazarganipour M, Noori E. Synthesis and characterization of spherical silica nanoparticles by modified Stöber process assisted by organic ligand. Superlattices Microstruct. 2013;61:33–41.
22. Zinatloo-Ajabshir S, Salavati-Niasari M. Facile route to synthesize zirconium dioxide (ZrO_2) nanostructures: structural, optical and photocatalytic studies. J Mol Liq. 2016;216:545–51.
23. Kalam A, Al-Sehemi AG, Assiri M, Du G, Ahmad T, Ahmad I, et al. Modified solvothermal synthesis of cobalt ferrite ($CoFe_2O_4$) magnetic nanoparticles photocatalysts for degradation of methylene blue with H_2O_2/visible light. Results Phys. 2018;8:1046–53.
24. Kurian J, Mathew MJ. Structural, optical and magnetic studies of $CuFe_2O_4$, $MgFe_2O_4$ and $ZnFe_2O_4$ nanoparticles prepared by hydrothermal/solvothermal method. J Magn Magn Mater. 2018;451:121–30.
25. Kanižaj L, Barišić D, Torić F, Pajić D, Molčanov K, Šantić A, et al. Structural, electrical, and magnetic versatility of the oxalate-based [CuFe] compounds containing 2,2′:6′,2″-terpyridine: anion directed synthesis. Inorg Chem. 2020;59:18078–89.
26. Habjanič J, Jurić M, Popović J, Molčanov K, Pajić D. A 3D oxalate-based network as a precursor for the $CoMn_2O_4$ spinel: synthesis and structural and magnetic studies. Inorg Chem. 2014;53:9633–43.
27. Jurić M, Pajić D, Žilić D, Rakvin B, Molčanov K, Popović J. Magnetic order in a novel 3D oxalate-based coordination polymer $\{[Cu(bpy)_3][Mn_2(C_2O_4)_3]\cdot H_2O\}_n$. Dalton Trans. 2015;44:20626–35.
28. Popović J, Jurić M, Pajić D, Vrankić M, Zavašnik J, Habjanič J. Effect of the cation distribution and microstructure on the magnetic behavior of the $CoMn_2O_4$ oxide. Inorg Chem. 2017;56:3983–9.
29. Mohammadnezhad G, Amini MM, Khavasi HR. A single source precursor for low temperature processing of nanocrystalline $MgAl_2O_4$ spinel: synthesis and characterization of $[MgAl_2(\mu_3\text{-}O)(\mu_2\text{-}O^iPr)_4(O^iPr)_2]_4$. Dalton Trans. 2010;39:10830–2.
30. Mahata P, Sarma D, Madhu C, Sundaresen A, Natarajan S. $CoMn_2O_4$ spinel from a MOF: synthesis, structure and magnetic studies. Dalton Trans. 2011;40:1952–60.
31. Androš L, Jurić M, Popović J, Šantić A, Lazić P, Benčina M, et al. $Ba_4Ta_2O_9$ oxide prepared from an oxalate-based molecular precursor—characterization and properties. Inorg Chem. 2013;52:14299–308.
32. Androš Dubraja L, Pajić D, Vrankić M, Dragović J, Valant M, Benčina M, et al. Single-step preparation of rutile-type $CrNbO_4$ and $CrTaO_4$ oxides from oxalate precursors–characterization and properties. J Am Ceram Soc. 2019;102:6697–704.
33. Androš L, Jurić M, Popović J, Pajić D, Zadro K, Molčanov K, et al. 1D heterometallic oxalate compounds as precursors for mixed Ca–Cr oxides – synthesis, structures, and magnetic studies. Eur J Inorg Chem. 2014;2014:5703–13.
34. Rietveld HM. A profile refinement method for nuclear and magnetic structures. J Appl Crystallogr. 1969;2:65–71.
35. Degen T, Sadki M, Bron E, König U, Nénert G. The HighScore suite. Powder Diffr. 2014;29:S13–S18.
36. Balagurov AM, Bobrikov IA, Maschenko MS, Sangaa D, Simkin VG. Structural phase transition in $CuFe_2O_4$ spinel. Crystallogr Rep. 2013;58:710–7.
37. Caglioti G, Paoletti A, Ricci P. Choice of collimators for a crystal spectrometer for neutron diffraction. Nucl Instrum Methods. 1958;3:223–8.
38. Hill RJ, Howard CJ. Quantitative phase analysis from powder diffraction data using the Rietveld method. J Appl Crystallogr. 1987;20:467–74.
39. Tauc J, Grigorovici R, Vancu A. Optical properties and electronic structure of amorphous germanium. Phys Status Solidi B. 1996;15:627–37.
40. López-Ramón MV, Álvarez MA, Moreno-Castilla C, Fontecha-Cámara MA, Yebra-Rodríguez Á, Bailón-García E. Effect of calcination temperature of a copper ferrite synthesized by a sol-gel method on its structural characteristics and performance as Fenton catalyst to remove gallic acid from water. J Colloid Interface Sci. 2018;511:193–202.
41. Calvo-de la Rosa J, Segarra M. Optimization of the synthesis of copper ferrite nanoparticles by a polymer-assisted sol–gel method. ACS Omega. 2019;4:18289–98.
42. Zakiyah LB, Saion E, Al-Hada NM, Gharibshahi E, Salem A, Soltani N, et al. Up-scalable synthesis of size-controlled copper ferrite nanocrystals by thermal treatment method. Mater Sci Semicond Process. 2015;40:564–9.
43. Javed R, Zia M, Naz S, Aisida SO, ul Ain N, Ao Q. Role of capping agents in the application of nanoparticles in biomedicine and environmental remediation: recent trends and future prospects. J Nanobiotechnol. 2020;18:172.
44. Solomon EI, Lever ABP. Inorganic electronic structure and spectroscopy. Hoboken, NJ: John Wiley & Sons, Inc.; 2006.
45. George P, Chowdhury P. Complex dielectric transformation of UV-vis diffuse reflectance spectra for estimating optical band-gap energies and materials classification. Analyst. 2019;144:3005–12.
46. Guijarro N, Bornoz P, Prévot M, Yu X, Zhu X, Johnson M, et al. Evaluating spinel ferrites MFe_2O_4 (M = Cu, Mg, Zn) as photoanodes for solar water oxidation: prospects and limitations. Sustainable Energy Fuels. 2018;2:103–17.
47. Trinh L, Bienkowski K, Wróbel P, Pisarek M, Parzuch A, Nawaz N, et al. New concept for the facile fabrication of core–shell CuO@$CuFe_2O_4$ photocathodes for PEC application. Materials. 2022;15:1029.
48. Ulpe AC, Bauerfeind KCL, Granone LI, Arimi A, Megatif L, Dillert R, et al. Photoelectrochemistry of ferrites: theoretical predictions vs. experimental results. Z Phys Chem. 2020;234:719–76.
49. Zhang Y-Q, Wang CC, Guo X-X, Wang P, Gao S-J. Two 1D coordination polymers constructed from 3,3’,4,4’-biphenyltetracarboxylic acid and 4,4’-bipyridine: hydrothermal syntheses and photocatalytic performance. Transition Met Chem. 2016;41:15–24.

50. Mahata P, Madras G, Natarajan S. Novel photocatalysts for the decomposition of organic dyes based on metal-organic framework compounds. J Phys Chem B. 2006;110:13759–68.
51. Dikhtiarenko A, Villanueva-Delgado P, Valiente R, García JR, Gimeno J. Tris(bipyridine)metal(II)-templated assemblies of 3D alkali-ruthenium oxalate coordination frameworks: crystal structures, characterization and photocatalytic activity in water reduction. Polymers. 2016;8:48.
52. Yuan C-M, Yan M-T, Yuan F, Ling X-Y, Zhou C-S, Wang J, et al. Synthesis and photocatalytic property of a new 1D metal–organic polymer. Inorg Chem Commun. 2019;108:107543.
53. Zhang Y-Q, Wang C-C, Guo X-X, Wang P, Gao S-J. Two 1D coordination polymers constructed from 3,3',4,4'-biphenyltetracarboxylic acid and 4,4'-bipyridine: hydrothermal syntheses and photocatalytic performance. Transition Met Chem. 2016;41:15–24.
54. Yuan F, Yuan C-M, Zhou C-S, Qiao C-F, Lu L, Ma A-Q, et al. Syntheses and photocatalytic properties of three new d10-based coordination polymers: effect of metal centre and ancillary ligands. CrystEngComm. 2019;21:6558–65.
55. Qian L-L, Wang Z-X, Zhu L-M, Li K, Li B-L, Wu B. Synthesis, structure, spectral characteristic and photocatalytic degradation of organic dyes of a copper metal-organic framework based on tri(triazole) and pimelate. Spectrochim Acta A. 2019;214:372–7.
56. Wang X, Sun J, Lin H, Chang Z, Liu G, Wang X. A series of novel Anderson-type polyoxometalate-based MnII complexes constructed from pyridyl-derivatives: assembly, structures, electrochemical and photocatalytic properties. CrystEngComm. 2017;19:3167–77.
57. Bhardwaj K. Potassium induced stitching of a flexible tripodal ligand into a bi-metallic two-dimensional coordination polymer for photo-degradation of organic dyes. Dalton Trans. 2015;44:8801–4.
58. Shilpa Amulya MA, Nagaswarupa HP, Anil Kumar MR, Ravikumar CR, Kusuma KB, Prashantha SC. Evaluation of bifunctional applications of $CuFe_2O_4$ nanoparticles synthesized by a sonochemical method. J Phys Chem Solids. 2021;148:109756.
59. Hariganesh S, Vadivel S, Paul B, Kumaravel M, Balasubramanian N, Rajendran S, et al. Metal organic framework derived magnetically recoverable $CuFe_2O_4$ porous cubes for efficient photocatalytic application. Inorg Chem Commun. 2021;125:108405.
60. Anandan S, Selvamani T, Guru Prasad G, Asiri AM, Wu JJ. Magnetic and catalytic properties of inverse spinel $CuFe_2O_4$ nanoparticles. J Magn Magn Mater. 2017;432:437–43.

SUPPORTING INFORMATION

Additional supporting information can be found online in the Supporting Information section at the end of this article.

How to cite this article: Molčanov L, Androš Dubraja L, Vrankić M, Jurić M. A 3D oxalate-bridged $[Cu^{II}Fe^{II}]$ coordination polymer as molecular precursor for $CuFe_2O_4$ spinel—photocatalytic features. J Am Ceram Soc. 2023;106:2997–3008. https://doi.org/10.1111/jace.18982